

1 **Tracking the Cracking: a Holistic Analysis of Rapid Ice**
2 **Shelf Fracture Using Seismology, Geodesy, and Satellite**
3 **Imagery on the Pine Island Glacier Ice Shelf, West**
4 **Antarctica**

5 **S. D. Olinger^{1,2}, B. P. Lipovsky², M. A. Denolle², B. W. Crowell²**

6 ¹Department of Earth and Planetary Sciences, Harvard University, Cambridge, Massachusetts, USA

7 ²Department of Earth and Space Sciences, University of Washington, Seattle, Washington, USA

8 **Key Points:**

- 9 • Fracture at PIG generate flexural gravity waves, a wave type related to interac-
10 tion between a floating plate and supporting fluid.
- 11 • Rift-tip seismicity rate increases with ice speed, either due to changes in the un-
12 derlying ice shelf stress state or localized thinning.
- 13 • Recorded flexural gravity waves are consistent with a point load of ~ 10 kPa ap-
14 plied over ~ 30 s, corresponding to ~ 10 m of vertical cracking.

Corresponding author: Seth D. Olinger, setholinger@fas.harvard.edu

15 **Abstract**

16 Ice shelves regulate the stability of marine ice sheets. We track fractures on Pine
 17 Island Glacier, a quickly-accelerating glacier in West Antarctica that contributes more
 18 to sea level rise than any other glacier. Using an on-ice seismic network deployed from
 19 2012 to 2014, we catalog icequakes that dominantly consist of flexural gravity waves. Ice-
 20 quakes occur near the rift tip and in two distinct areas of the shear margin, and TerraSAR-
 21 X imagery shows significant fracture in each source region. Rift-tip icequakes increase
 22 with ice speed, linking rift fracture to glaciological stresses and/or localized thinning. Us-
 23 ing a simple flexural gravity wave model, we deconvolve wave propagation effects to es-
 24 timate icequake source durations of 19.5 to 50.0 s, and transient loads of 3.8 to 14.0 kPa
 25 corresponding to 4.3 to 15.9 m of crevasse growth per icequake. These long source du-
 26 rations suggest that water flow may limit the rate of crevasse opening.

27 **1 Plain Language Summary**

28 Large shelves of floating ice strengthen glaciers in Antarctica, helping to protect
 29 against rapid sea level rise that can occur when glaciers flow into the ocean. Ice shelves
 30 can collapse through rapid cracking (synonym of fracturing), but it is difficult to directly
 31 observe cracking on ice shelves. In this paper, we track cracks on Pine Island Glacier,
 32 an ice shelf in Antarctica that is particularly vulnerable to collapse. We see cracks in pic-
 33 tures taken by satellites. Cracking causes the ice shelf to shake up and down, which we
 34 record using the same equipment that records earthquakes. We record shaking located
 35 at a set of cracks at the side of the ice shelf and at the tip of a single massive crack called
 36 a rift. Rift cracking seems related to the speed that the ice shelf is flowing. We also use
 37 a computer simulation of shaking to learn about the details of the crack process. Our
 38 simulation suggests that the crack process might be more complicated than a single crack
 39 opening evenly at a constant rate.

40 **2 Introduction**

41 Ice shelf fracture exerts a fundamental control on the stability of marine ice sheets
 42 and associated sea level fluctuations (Seroussi et al., 2020). In particular, understand-
 43 ing the past, present, and future stability of the West Antarctic Ice Sheet (WAIS) re-
 44 mains one of the great challenges of modern glaciological research and is itself closely
 45 related to ice shelf fracturing processes (Scambos et al., 2017). Fractures on ice shelves
 46 take on many forms including through-cutting rifts (Larour et al., 2004; Hulbe et al., 2010;
 47 Lipovsky, 2020), smaller-scale basal and surface crevasses (Rist et al., 2002; McGrath
 48 et al., 2012), hydraulic fracturing (Weertman, 1973; Banwell et al., 2013), and cliff fail-
 49 ure (Clerc et al., 2019). Despite decades of progress, understanding of ice shelf fracture
 50 remains significantly hindered by a lack of direct observation (Benn et al., 2007). A num-
 51 ber of basic questions remain or have only partially been addressed: What forces are in-
 52 volved in ice shelf fracture? Is ice shelf fracture a fast and brittle or slow and ductile pro-
 53 cess? To what degree is water involved in fracture propagation? Does ice shelf fracture
 54 growth happen at a constant rate or in bursts, and what controls its timing?

55 All of these questions can be addressed using seismology. Because seismic waves
 56 carry information about the dynamics of fracture, numerous previous studies have lever-
 57 aged such signals, often referred to as icequakes, for this purpose (Von der Osten-Woldenburg,
 58 1990; Hammer et al., 2015; Chen et al., 2019; Winberry et al., 2020). Seismic studies on
 59 ice shelves have shown that crevasse propagation is intermittent (Bassis et al., 2007; Heeszel
 60 et al., 2014) and have highlighted environmental forcings that would be difficult to as-
 61 certain using only remotely sensed observations (Bassis et al., 2008; Olinger et al., 2019;
 62 Aster et al., 2021).

63 Here, we use seismic recordings to quantify fracturing of the Pine Island Glacier
64 (PIG) Ice Shelf. PIG, itself part of the larger WAIS, contributes more to present day global
65 sea level rise than any other glacier (Shepherd et al., 2018). Ice mass loss on PIG is thought
66 to be due to the retreat of the floating ice shelf (Joughin, Shapero, Smith, et al., 2021),
67 the latter being caused by interactions between ocean forcing (Christianson et al., 2016;
68 Joughin, Shapero, Dutrieux, & Smith, 2021) and fracturing processes (MacGregor et al.,
69 2012).

70 We focus on icequakes that travel as flexural gravity waves to quantify fracturing
71 of PIG Ice Shelf. Flexural gravity waves are a type of hybrid seismic-water wave (Ewing
72 & Crary, 1934) unique to floating structures such as ice shelves since both elasticity and
73 buoyancy act as their restoring force (Ewing & Crary, 1934). Flexural gravity waves are
74 strongly dispersive (Ewing & Crary, 1934), which can make waveform analysis difficult
75 and necessitates careful modelling (Sergienko, 2017; Mattsson et al., 2018; Lipovsky, 2018).
76 Despite this challenge, flexural gravity waves are useful tools to study ice shelf processes
77 because, while direct body waves in ice shelves are often not observed at distances greater
78 than a few ice thickness (Zhan et al., 2014), flexural gravity waves are often observed to
79 travel long distances from their exciting source (Williams & Robinson, 1981).

80 Many sources have been observed to generate flexural gravity waves on ice shelves
81 including ocean swell (Williams & Robinson, 1981), tsunamis (Bromirski et al., 2017),
82 and airplane landings (MacAyeal et al., 2009). MacAyeal et al. (2009) appears to have
83 been the first to propose that fracturing processes in ice shelves may act as seismic sources
84 that generate flexural gravity waves. MacAyeal et al. (2009) considered water motion
85 in a deforming rift and motion of detaching blocks from the ice front as two such sources.
86 Here, we hypothesize that crevasse growth generates flexural gravity waves.

87 We begin our fracture analysis by describing a timeline of events with the use of
88 satellite imagery. Next, we create a catalog of flexural gravity waves on PIG to exam-
89 ine the relationship between crack growth, large-scale rift propagation, shear margin pro-
90 cesses, and ice shelf acceleration. We then interrogate icequake source physics by mod-
91 eling the ice shelf as a buoyantly supported beam, the simplest model that captures flex-
92 ural gravity wave propagation (Sergienko, 2017; Mattsson et al., 2018). Because this model
93 only has the vertical component motion as an independent variable, classical dislocations
94 require an indirect parameterization in terms of either vertical motion or one of its deriva-
95 tives (Hetenyi, 1946). In our analysis, we model flexural gravity wave generation by a
96 point load or bending moment applied during ice shelf crevasse growth to infer key source
97 parameters of the recorded icequakes.

98 **3 Analysis of Satellite Imagery and Positioning**

99 We track visible fracturing on PIG using images collected by the TerraSAR-X satel-
100 lite (Pitz & Miller, 2010) from 2012 to 2014. At the start of our study period in January
101 2012, the primary visible fractures are the rift, ~ 20 large cracks extending into the ice
102 shelf from northern shear margin, and ~ 10 cracks extending into the ice shelf at the south-
103 ern edge of the nascent iceberg (Figure 1a, left). By January 2013, the rift had propa-
104 gated a few kilometers without significant widening, and two wing cracks (Renshaw &
105 Schulson, 2001) opened at the rift tip (Figure 1a, right). One of the cracks at the north-
106 ern shear margin extended 7 km and connected to the rift between May 8 and May 11,
107 2012. The other northern shear margin cracks extended and widened, at least two new
108 cracks initiated near Evans Knoll, and one of cracks at the southern edge of the nascent
109 iceberg extended to within a kilometer of the rift tip.

110 During the first four months of 2013, the wing cracks near the rift tip extended and
111 widened. In early July 2013, a block of ice calved along a wing crack at the southern edge
112 of the nascent iceberg near the rift tip (Figure 1b). After this preliminary calving event,

113 the only connection between the nascent iceberg and the ice shelf was a 2 km wide strip
114 of ice between the ocean and a wing crack. Over the next few months, we observe sig-
115 nificant widening of the rift, likely due to the iceberg beginning to drift away from the
116 ice shelf. Iceberg B-31 calved in November 2013 (Figure 1c) when left lateral motion of
117 the iceberg pried open a large wing crack near the rift tip until a strip of ice stabilizing
118 the iceberg broke off, allowing Iceberg B-31 to drift into the sea. By the end of 2013, many
119 fractures in the northern shear margin had extended and calved smaller icebergs, and
120 several new fractures had initiated near Evans Knoll.

121 We furthermore examine Global Positioning System (GPS) speed timeseries derived
122 from five continuous GPS stations. The GPS stations were co-located with seismome-
123 ters (locations shown in Figure 2). Our GPS processing is described in Supporting Text
124 S1. Figure 3a plots the GPS-derived ice shelf speed. We find that ice speed at PIG de-
125 creases from 11.1 m/day in January 2012 to 10.8 m/day in April 2013. Then, ice speed
126 drops to below 10.6 m/day for eight days in early May 2013. Following this rapid slow-
127 down, ice speed begins to increase, reaching 10.9 m/day by the end of 2013. The GPS
128 ice speed we compute here is consistent with a previous study utilizing the same dataset
129 (Christianson et al., 2016).

130 4 Analysis of Seismograms

131 We examine seismic data from five sites on PIG (Stanton et al., 2013). The instru-
132 ments were deployed in January 2012 and retrieved in December 2013, providing two years
133 of continuous data. The seismic stations were deployed in a cross shape with 5 km aper-
134 ture at the center of the ice shelf (Figure 2). Each site consisted of a three component
135 Nanometrics Trillium 120 Broadband seismometer and a Quanterra Q330 digitizer (David
136 Holland & Robert Bindschadler, 2012). Seismic data was sampled at 100 Hz, and we re-
137 moved the instrumental response on the frequency band 0.001 Hz to 45 Hz.

138 In the seismic dataset, we observe events with an abrupt onset and with high fre-
139 quencies that arrive before low frequencies. This type of dispersion is characteristic of
140 flexural gravity waves. The observed dispersion (high frequency waves travel faster) is
141 the opposite of typical surface waves in the solid Earth. In the latter case, low frequency
142 waves travel faster because seismic wave speeds generally increase with depth.

143 To detect flexural gravity waves in the dataset, we design a two-stage detection scheme
144 that identifies broadband, dispersive seismic events. Our detection approach, detailed
145 in Text S2, uses a dual-band short term average/long term average (STA/LTA) detec-
146 tor in combination with template matching (Allen, 1978; Gibbons & Ringdal, 2006). This
147 detection approach results in a preliminary catalog of 22,119 events. Inspection of the
148 preliminary catalog reveals two main families of events: one with clear high-frequency-
149 first dispersion and one which is dominantly monochromatic. In order to focus on flex-
150 ural gravity waves, we undertake waveform clustering using a K-Shape algorithm (Paparrizos
151 & Gravano, 2016) modified to operate on multi-component seismic data. Visual anal-
152 ysis of the clustered catalog demonstrates the efficacy of our approach in isolating flex-
153 ural gravity waves (Figure 3). Our final catalog contains 8,184 likely flexural gravity wave
154 events. For simplicity, in the rest of the text we refer to flexural gravity wave events as
155 icequakes.

156 We next determine locations for all icequakes in our final catalog. Given the poor
157 distribution of the stations with respect to fracture locations, we employ single-station
158 approaches to locating icequakes. We compute epicentral back-azimuths by analyzing
159 the polarization direction of recorded horizontal waves (Aster et al., 2021). We apply prin-
160 ciple component analysis (PCA) to the horizontal component seismograms to retrieve
161 polarization directions. The polarization provides a 180 degree ambiguity, so we find the
162 direction of propagation based on which station recorded the first arrival (see Text S3).

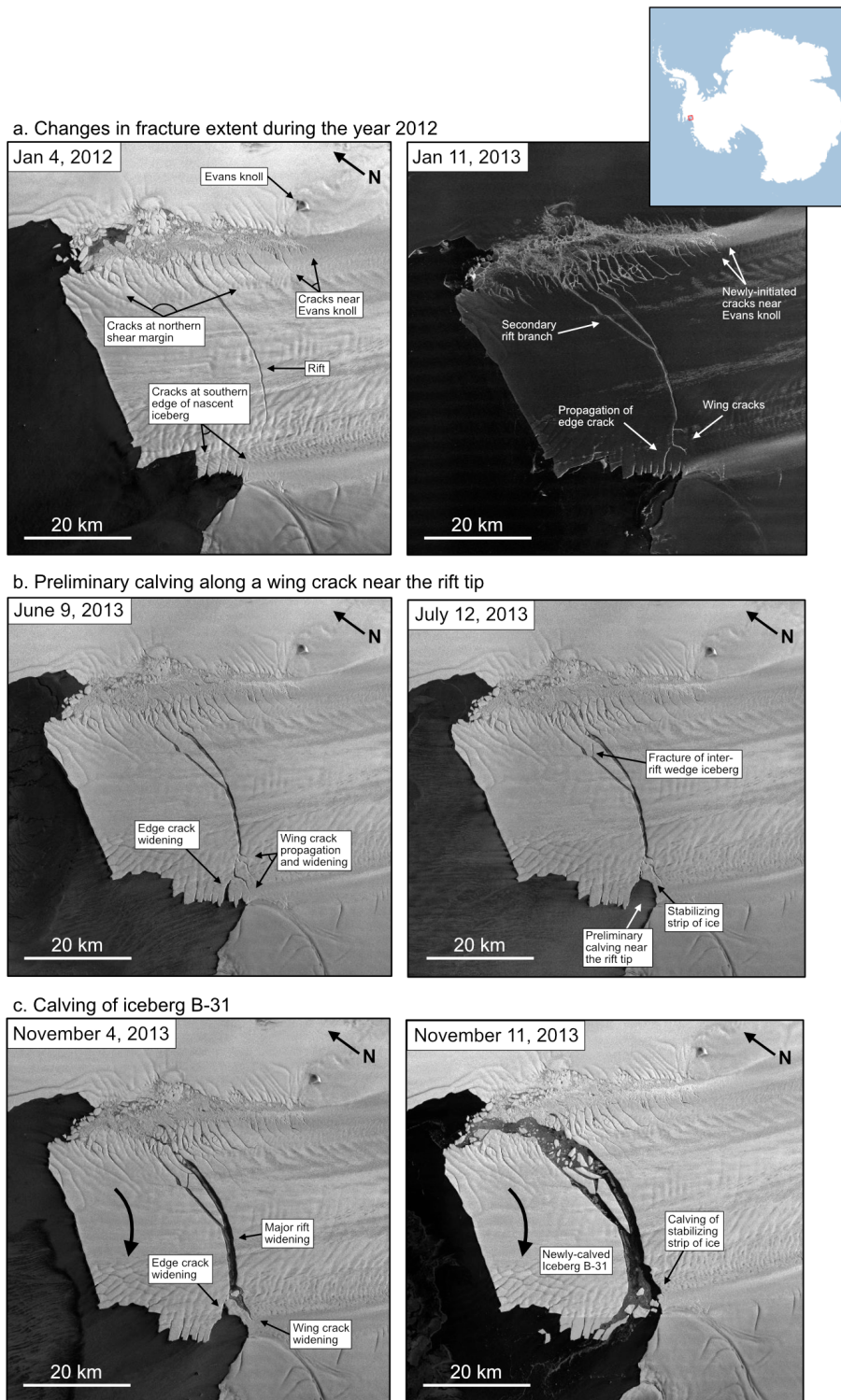


Figure 1. TerraSAR-X images showing an overview of fracture development at PIG from 2012 to 2014. Large arrow in panels c. and d. show sense of motion of the iceberg. See text for full discussion. Inset shows the location of PIG in Antarctica.

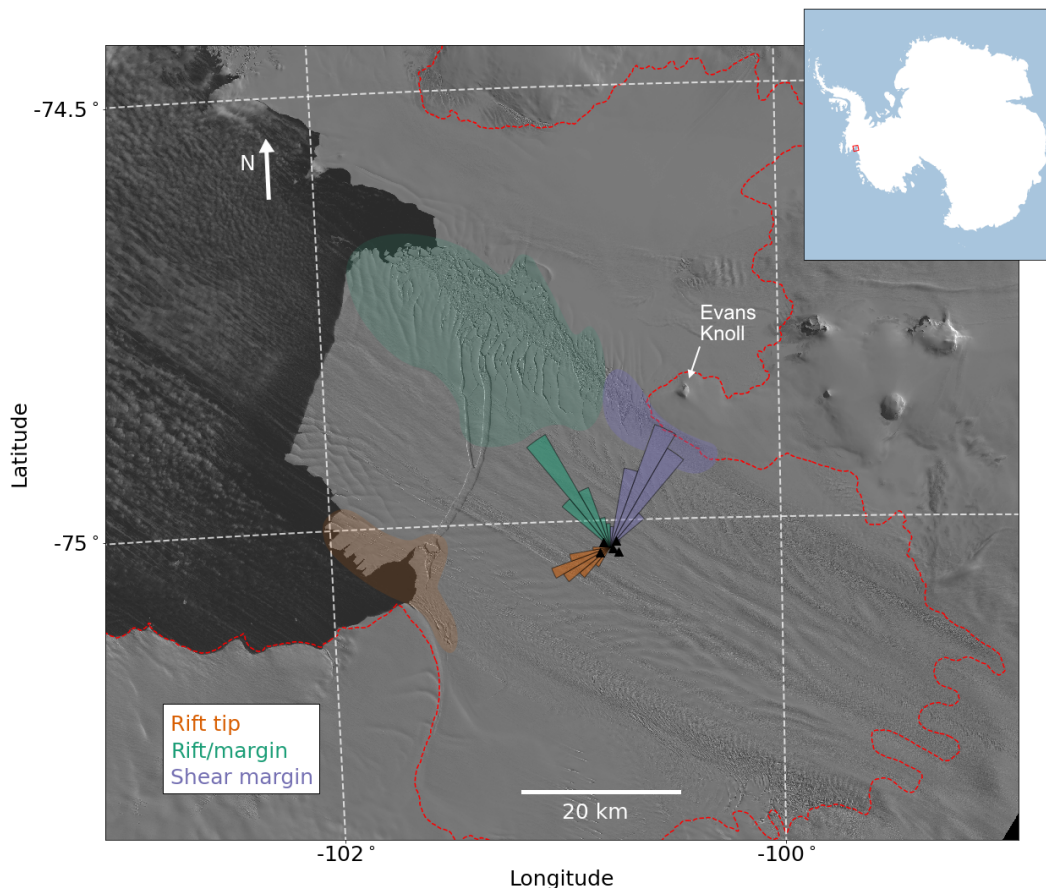


Figure 2. Back-azimuthal histogram showing locations of cataloged icequake. Rift-tip event back-azimuths are plotted as orange rays. Rift/margin-event back-azimuths are plotted as purple rays. Shear-margin event back-azimuths are plotted as green rays. Likely source regions are shown by colored polygons. PIG array seismic and GPS stations are plotted as black triangles. Approximate grounding line position is shown by the red dashed line (Bindschadler et al., 2011). Background LANDSAT imagery is from October 2013 (courtesy of the United States Geological Survey).

163 We locate all of the 8,184 icequakes to one of three distinct source regions: the rift
 164 tip, the body of the rift and nearby shear margin (“rift/margin”), and the northeast shear
 165 margin near Evan’s knoll (“shear margin”), which are depicted in Figure 2. These spa-
 166 tial groups correspond to 22%, 29%, and 40% of the catalog, respectively, with 9% of events
 167 having indeterminate locations. Figure 2 shows the back-azimuthal histograms of the
 168 three groups.

169 5 Relationships Between Icequakes and Ice Shelf Behavior

170 5.1 Rift tip

171 The rift-tip icequakes are coincident in space and time with several fracturing pro-
 172 cesses including rift propagation, wing cracking, small scale calving within the rift, and
 173 calving along the southern edge of the nascent iceberg. Rift tip events occurred more

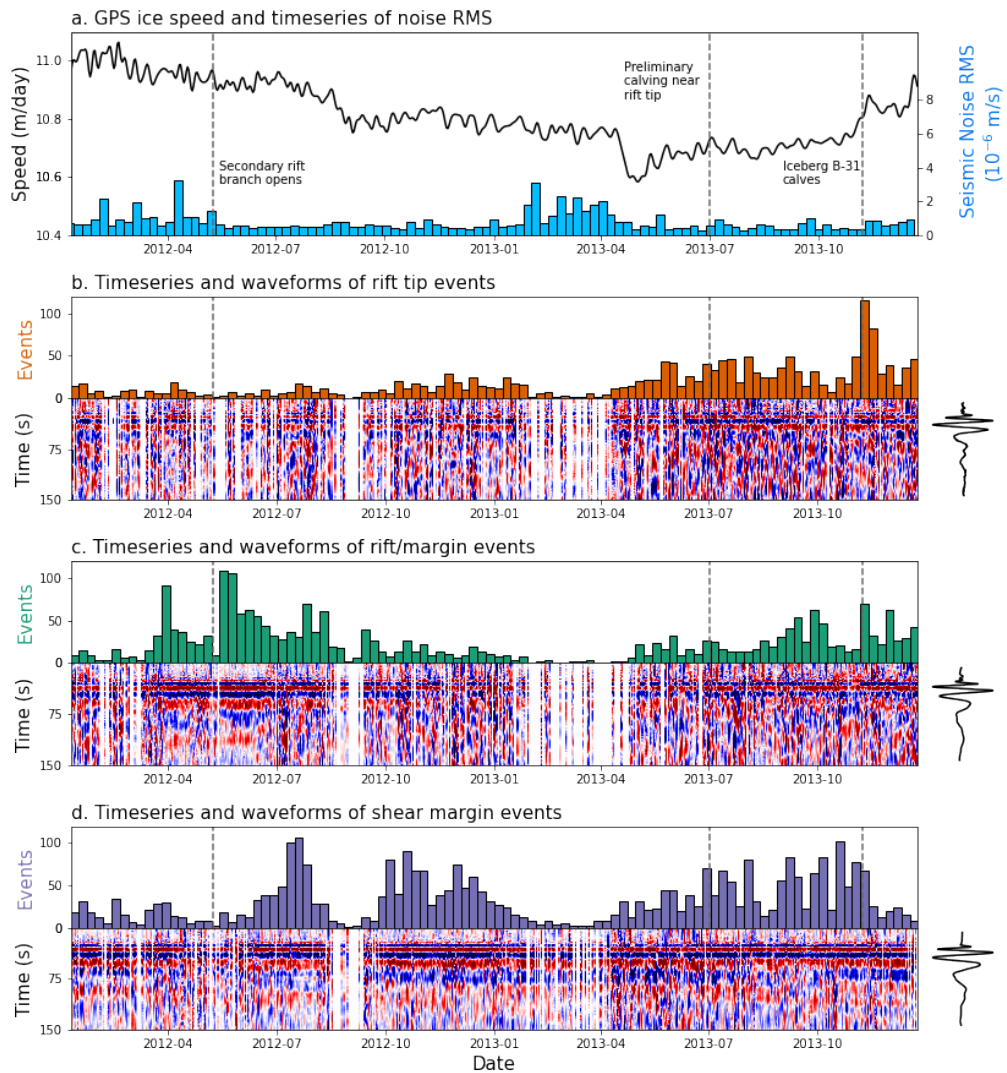


Figure 3. Timing and waveforms of cataloged icequake. (a) GPS-derived ice velocity is shown by the black line, and average seismic noise is shown by blue bars. Noise is highest in the Antarctic summer, when minimal sea ice is present to attenuate ocean-generated noise, reducing detectability in January, February, and March. (b) Rift-tip events. Weekly timeseries of rift tip event times is shown by orange bars. Daily vertical (HHZ) waveform stacks of detected rift tip events are plotted beneath. Overall rift-tip event stack is shown to the right. (c) Same as (b) for northwest shear-margin events, color-coded in green. (d) Same as (b) for northeast shear-margin events, color-coded in purple.

174 frequently in 2013 than in 2012 (Figure 3b). The mean seismicity rate was 9.4 icequakes/week
 175 in 2012 and 25.6 icequakes/week in 2013. 19 weeks of 2013 equaled or exceeded the max-
 176 imum 2012 seismicity rate of 29 icequakes/week. Weekly icequake counts increased past
 177 the peak level seen in 2012 on May 21, 2013 and remain elevated until the end of the de-
 178 ployment. This period of elevated rift tip seismicity corresponds to the phase of signif-
 179 icant wing crack growth and rift widening observed in imagery.

180 Peak levels of rift-tip seismicity were observed during the calving of Iceberg B-31
 181 in the week of November 5, 2013. That week had 115 rift-tip events, the highest event
 182 count of any week across all three source regions. Furthermore, elevated rift-tip icequake
 183 activity in 2013 corresponds to a period of accelerating ice velocities (Figure 3a). While
 184 rift-tip fracture may be more directly related to strain rate in a viscous regime and strain
 185 in an elastic regime, we simply note that ice speed reflects the underlying stress state
 186 of the ice shelf. The correspondence in time between elevated rift-tip seismicity rates and
 187 increasing ice velocities therefore suggests that rift propagation is sensitive to the un-
 188 derlying stress state of the ice shelf. In addition, rift tip fracture may be enhanced by
 189 localized ice shelf thinning and melt within the rift. Christianson et al. (2016) hypoth-
 190 esize that the overall pattern of ice velocities at PIG in 2013 tracks a time-lagged response
 191 to ocean melting, and localized melt has been proposed as a primary driver of rifting at
 192 PIG (Walker & Gardner, 2019; Jeong et al., 2016). The observed connection in time be-
 193 tween rift tip fracture and accelerated ice velocities demonstrates that rift growth and
 194 PIG is sensitive to changes in ice dynamics, localized melt, or a combination of both. At
 195 the present time, however, we are unable to confirm whether local or more distant melt-
 196 related feedbacks are responsible for the observed fracturing.

197 5.2 Rift/margin

198 The rift/margin icequakes are coincident in space and time with the growth of ~ 20
 199 rifts formed in the northwest shear zone, as well as smaller-scale fractures and widen-
 200 ing of the main rift itself. Rift/margin icequakes occurred more frequently in 2012 than
 201 in 2013. The mean seismicity rate was 27.7 icequakes/week in 2012 and 19.3 icequakes/week
 202 in 2013. Four weeks of 2012 equaled or exceeded the maximum 2013 seismicity rate of
 203 70 icequakes/week. The timing of icequakes in the rift/margin group is independent of
 204 ice speed. Peak levels of rift/margin seismicity were observed during the week of May
 205 15, 2012, which contained 109 rift/margin icequakes. Rift/margin icequakes reach peak
 206 seismicity rates in the weeks following the opening of the secondary rift branch in May
 207 2012, suggesting that the crack opening caused aftershock-like seismicity and/or desta-
 208 bilized the margin, enhancing the growth of nearby fractures.

209 5.3 Shear margin

210 The shear-margin icequakes are coincident in space and time with the initiation
 211 of new cracks and growth of extant cracks near Evans Knoll. This area marks the tran-
 212 sition from a primarily intact shear margin upstream of Evans Knoll to a highly frac-
 213 tured shear margin downstream of Evans Knoll. Imagery shows that multiple fractures
 214 longer than 1 km were initiated in this area during 2012 and 2013 (Figure 1). Shear-margin
 215 icequakes occurred at an approximately equal rate in 2012 and 2013. The mean seismic-
 216 ity rate was 31.9 icequakes/week in 2012 and 32.2 icequakes/week in 2013. Peak levels
 217 of shear margin seismicity were observed during the week of July 17, 2012, which con-
 218 tained 107 shear-margin icequakes. Shear-margin icequakes do not exhibit any promi-
 219 nent temporal trends and appear independent of ice velocity. The shear margin expe-
 220 riences the highest overall level of seismic activity, suggesting that the transition point
 221 from intact to fractured ice near Evans Knoll experiences higher stress concentrations
 222 than either the rift tip or the rift/margin regions, consistent with rift modeling (Lipovsky,
 223 2020).

224

6 Icequake Source Analysis

We next estimate the distribution of forces that gives rise to the observed seismograms. We do this by removing wave propagation effects from the observed seismograms using a numerically computed Green's function. Our catalog was designed to represent icequakes that mostly consist of flexural gravity waves. We therefore model the vertical seismograms using the simplest model that gives rise to flexural gravity waves, the dynamic floating beam equation (Ewing & Crary, 1934; Squire & Allan, 1977),

$$\rho_i h_i \frac{\partial^2 w}{\partial t^2} + D \frac{\partial^4 w}{\partial x^4} + \rho_w g w + \rho_w \frac{\partial \phi}{\partial t} = P, \quad (1)$$

225

226

227

228

229

230

231

232

233

where $D \equiv EI = Eh_i^3/[12(1-\nu^2)]$ is the flexural rigidity with second moment of area $I = \int_{-h_i/2}^{h_i/2} z^2 dz$, E is the Young's modulus of ice, ν is the Poisson's ratio of ice, t is time, x is horizontal position, g is gravitational acceleration constant, h_i is the ice thickness, ρ_i is the density of ice, ρ_w is the density of water, w is the vertical displacement of the beam, ϕ is the ocean surface velocity potential, and P is an applied point load. From left to right, the terms in Equation (1) represent inertia, flexure of the ice shelf, buoyancy, and ocean surface waves generated at the ice-water interface. We initially use a locally-averaged ice thickness of $h_i = 400$ m (Shean et al., 2019) and a water depth of $h_w = 590$ m (Fretwell et al., 2013).

234

235

236

237

238

239

240

241

242

243

244

245

246

247

We model icequake sources as either an applied point load or point bending moment. When a basal crevasse opens and fills with water, the downward-acting ice overburden stress at the top of the crevasse is greater in magnitude than the upward-acting buoyancy stress exerted by water filling the crevasse. This applies a downward point load to the ice shelf. In addition, the horizontal ice overburden stress along the walls of the crevasse is greater in magnitude than the horizontal buoyancy stress exerted by the water filling the crevasse. The difference in magnitude between these two stresses decreases with depth such that the walls of a crevasse are subject to stress gradient. This applies a bending moment to the ice shelf. These two mechanisms may also act in concert and simultaneously apply a moment and point load to the ice shelf. We choose not to pursue such hybrid sources at the present time, however, because the simplicity of our model—specifically the assumptions of uniform ice thickness and two-dimensional geometry—suggests that additional source complexity is not warranted prior to improvements in these other areas.

248

249

250

251

252

253

254

We obtain the Green's function of the floating beam equation as the impulse response of the mechanical system to a point load (force per unit length) source. Rewriting Equation 1 using the linear operator \mathcal{A} as $\mathcal{A}w = P$, the Green's function equation can then be written as $\mathcal{A}G = \delta(x)\delta(t)$. In Supporting Text S4, we derive a frequency-wavenumber solution for G that we are able to analytically invert in the time domain and numerically invert in the frequency domain. We then derive G_m , the vertical displacement response to a point moment source.

255

256

257

258

259

260

We deconvolve G and G_m from waveform stacks to estimate the source load or moment distribution of events in each spatial group. Figure 4 shows our deconvolution result for the rift-tip icequakes, illustrating that a given vertical displacement seismogram may equivalently be represented as a point moment (Figure 4a and b) or a point load (Figure 4c and d). The equivalent analysis for the other two groups of events is given in Supporting Figures S1-2.

261

262

263

264

265

266

We examine the sensitivity of our deconvolution to the assumed value for the ice thickness by varying the ice thickness between 300 and 500 m (Figures S3-5). For the rift-tip group, we find source durations ranging from 30.48 to 50.00 s and amplitudes ranging from 2.69 to 6.90 MPa-m (point moment) and 3.83 to 8.62 kPa (point load). For the rift/margin group, we find source durations ranging from 19.52 to 48.57 s and amplitudes ranging from 3.82 to 12.55 MPa-m (point moment) and from 5.05 to 14.02 kPa (point

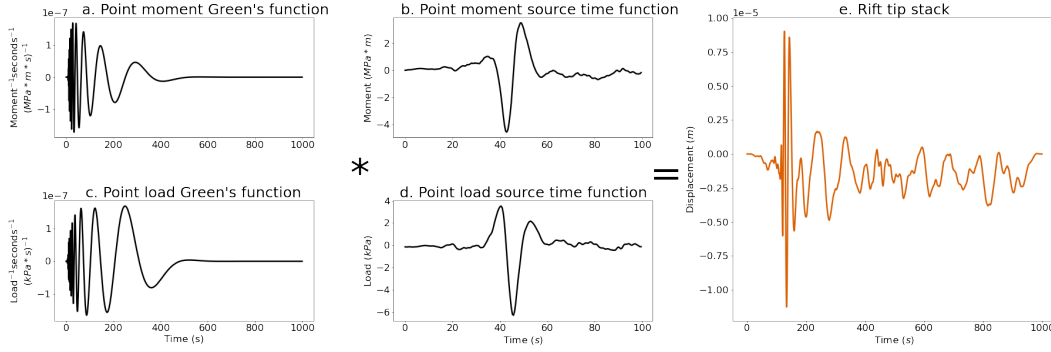


Figure 4. Green's functions and source time functions for rift tip events. (a) Theoretical Green's function for a point moment source located at a distance of 25 km, which is approximately the distance from PIG seismic array to the rift tip. (b) Source time function retrieved by deconvolving the point moment Green's function from the stack of rift tip vertical displacement waveforms. (c) Theoretical Green's function for a point load source located at a distance of 25 km. (d) Source time function retrieved by deconvolving the point load Green's function from the stack of rift tip vertical displacement waveforms. (e) Stack of rift tip vertical displacement waveforms obtained by aligning waveforms to a master event and taking the mean waveform on the frequency band 0.01-1 Hz.

267 load). Finally, for the shear-margin group, we find source durations ranging from 27.14
 268 to 36.67 s and amplitudes ranging from 5.60 to 14.89 MPa·m (point moment) and from
 269 8.04 to 12.97 kPa (point load).

270 7 Discussion of icequake source physics

271 How large were the cracks that generated the recorded flexural gravity waves? We
 272 estimate the amount of vertical crack opening for each spatial group using the point load
 273 source amplitudes (Text S5) for ice thickness varying between 300 and 500 m. Rift tip
 274 point load amplitudes correspond to 4.3 to 9.8 m of vertical crevasse opening. Rift/margin
 275 point load amplitudes correspond to 5.7 to 15.9 m of vertical crevasse opening. Shear-
 276 margin point load amplitudes correspond to 9.1 to 14.7 m of vertical crevasse opening.
 277 This suggests that the large-scale fracture opening and rift propagation observed in im-
 278 agery (Figure 1) was the result of many discrete crack opening events that each spanned
 279 only about 1 % of the ice thickness, not the result of full-thickness crack opening. Bassis
 280 et al. (2007) and Heeszel et al. (2014) observed episodic rift seismicity on the Amery Ice
 281 Shelf and proposed that rifts might propagate due to the coalescence of smaller cracks.
 282 Our findings support the hypothesis that crack coalescence can act as a mechanism of
 283 rifting.

284 Estimated source time series for moment and point load exhibit one or several pulses
 285 of activity followed by a return to zero (Figure 4). Source time functions derived from
 286 body waves in an elastic medium result in estimates of moment rate (Aki & Richards,
 287 2002, Equation 4.32,). Here, however, our deconvolution is sensitive not to the rate of
 288 change of point load or moment, but instead to a point load and moment. This compli-
 289 cates the interpretation of the estimated source time series because it suggests that the
 290 icequakes represent the application and subsequent removal of some point load or mo-
 291 ment. This physically counterintuitive situation motivates an examination of the sensi-
 292 tivity of our deconvolution to static offsets. We therefore calculate synthetic seismo-
 293 grams forced by a step in moment or point load (Figures S6-S8). We find that in some

294 cases the step function provides an acceptable fit to the observations. We therefore are
 295 unable to infer whether the observed flexural gravity waves were generated by a pulse-
 296 like or step-like source.

297 The timescale of the source process, however, is constrained independent of the ex-
 298 act force distribution assumed in the deconvolution. Our source analysis implies that the
 299 recorded flexural gravity waves were generated by fracturing process with approximately
 300 20-50 s duration. At this timescale, the observed waves must have been generated by brittle
 301 fracture, not by viscous deformation. This 20-50 s timescale is extremely slow com-
 302 pared, for example, to tectonic earthquakes, where earthquake duration scales like $10^{M/2}$
 303 with earthquake moment M and 20 s duration is associated with a $M = 7$ earthquake
 304 (Ekström et al., 2003).

305 What process sets the duration of the observed icequakes? The above scaling for
 306 tectonic earthquakes is based on the reasoning that the duration is set by the time re-
 307 quired for a shear crack to propagate across a fault of length L at a rate that tends to-
 308 wards inertial velocities (either the shear or dilatational wave speed v_s or v_p) (Freund,
 309 1998). In our system, however, we expect that water plays a limiting role in the speed
 310 of fracture propagation that may not be present in tectonic earthquakes. The propaga-
 311 tion of fluid filled basal crevasses is expected to occur at the crack wave speed (Lipovsky
 312 & Dunham, 2015). The crack wave speed is much slower than the inertial velocities and
 313 could plausibly be in the range of 1-100 m/s for basal crevasses in ice shelves. These ve-
 314 locities would suggest source length scales on the order of meters to hundreds of meters.
 315 A second plausible explanation is that long durations may be explained by the coales-
 316 cence of many smaller individual fractures that open successively. And yet another ex-
 317 planation is that there could be significant horizontal propagation which is not captured
 318 in our model. We expect that more detailed near-source observations would be able to
 319 distinguish between these possible scenarios.

320 8 Conclusions

321 We detect and locate icequakes that propagate as flexural gravity waves on the Pine
 322 Island Glacier ice shelf from 2012 to 2014. When compared to satellite imagery, the back-
 323 azimuthal distribution of the detected events suggests that the icequakes were generated
 324 by fractures at the tip of a large rift and in two distinct portions of the northern shear
 325 margin. Most of the events were generated at the shear margin near Evans Knoll, in agree-
 326 ment with imagery that suggests significant fracture initiation. Increased fracturing at
 327 the rift tip is associated with increased ice speed and elevated basal melting in 2013(Christianson
 328 et al., 2016). We attribute this relationship to changes in the stress state of the ice shelf
 329 or to melt-driven thinning that elevated rift tip stress concentrations. We use a simple
 330 model of flexural gravity waves to constrain the source of the recorded waves. We find
 331 that the observed waves have a source duration between 20-50 s. This timescale implies
 332 that a brittle fracture process generated the waves. Our analysis therefore confirms the
 333 role of brittle processes in the long-term evolution of marine ice sheets.

334 Acknowledgments

335 SDO and BPL were supported by the National Science Foundation (NSF) Office of Pol-
 336 ar Programs (OPP) award #1853896. SDO was also supported by startup funds of MAD
 337 at Harvard University in the Department of Earth and Planetary Sciences. The facil-
 338 ities of IRIS Data Services and IRIS Data Management Center were used for access to
 339 waveforms, metadata, and/or derived products used in this study. IRIS Data Services
 340 are funded through the Seismological Facilities for the Advancement of Geoscience (SAGE)
 341 Award of the National Science Foundation under Cooperative Support Agreement EAR-
 342 1851048. The seismic and geodetic datasets were collected by David Holland and Robert
 343 Bindschadler (2012), and the seismic DOI is <https://doi.org/10.7914/sn/xc.2012>.

344 Seismic instruments were provided by the Incorporated Research Institutions for Seis-
 345 mology (IRIS) through the PASSCAL Instrument Center at New Mexico Tech. Data col-
 346 lected is available through the IRIS Data Management Center. The facilities of the IRIS
 347 Consortium are supported by the National Science Foundation’s Seismological Facilities
 348 for the Advancement of Geoscience (SAGE) Award under Cooperative Support Agree-
 349 ment EAR-1851048. Geodetic data are based on services provided by the GAGE Facil-
 350 ity, operated by UNAVCO, Inc., with support from the National Science Foundation and
 351 the National Aeronautics and Space Administration under NSF Cooperative Agreement
 352 EAR-1724794. GPS processing was done using the GipsyX software, licensed to BWC
 353 at University of Washington. TerraSAR-X images were obtained using the freely-available
 354 EOWEB GeoPortal courtesy of the German Aerospace Center (DLR). Code to repro-
 355 duce the processing workflow for this paper is hosted at <https://zenodo.org/badge/latestdoi/468875023>.

356 References

- 357 Aki, K., & Richards, P. G. (2002). *Quantitative seismology*.
- 358 Allen, R. V. (1978, 10). Automatic earthquake recognition and timing from sin-
 359 gle traces. *Bulletin of the Seismological Society of America*, 68(5), 1521-1532.
 360 Retrieved from <https://doi.org/10.1785/BSSA0680051521> doi: 10.1785/
 361 BSSA0680051521
- 362 Aster, R. C., Lipovsky, B. P., Cole, H. M., Bromirski, P. D., Gerstoft, P., Nyblade,
 363 A., ... Stephen, R. (2021). Swell-triggered seismicity at the near-front damage
 364 zone of the ross ice shelf. *Seismological Research Letters*.
- 365 Banwell, A. F., MacAyeal, D. R., & Sergienko, O. V. (2013). Breakup of the larsen b
 366 ice shelf triggered by chain reaction drainage of supraglacial lakes. *Geophysical*
 367 *Research Letters*, 40(22), 5872–5876.
- 368 Bassis, J. N., Fricker, H. A., Coleman, R., Bock, Y., Behrens, J., Darnell, D.,
 369 ... Minster, J.-B. (2007). Seismicity and deformation associated with
 370 ice-shelf rift propagation. *Journal of Glaciology*, 53(183), 523–536. doi:
 371 10.3189/002214307784409207
- 372 Bassis, J. N., Fricker, H. A., Coleman, R., & Minster, J.-B. (2008). An inves-
 373 tigation into the forces that drive ice-shelf rift propagation on the amery
 374 ice shelf, east antarctica. *Journal of Glaciology*, 54(184), 17–27. doi:
 375 10.3189/002214308784409116
- 376 Benn, D. I., Warren, C. R., & Mottram, R. H. (2007). Calving processes and the dy-
 377 namics of calving glaciers. *Earth-Science Reviews*, 82(3-4), 143–179.
- 378 Bindschadler, R., Choi, H., Wichlacz, A., Bingham, R., Bohlander, J., Brunt, K.,
 379 ... Young, N. (2011). Getting around antarctica: new high-resolution map-
 380 pings of the grounded and freely-floating boundaries of the antarctic ice sheet
 381 created for the international polar year. *The Cryosphere*, 5(3), 569–588. Re-
 382 trieved from <https://tc.copernicus.org/articles/5/569/2011/> doi:
 383 10.5194/tc-5-569-2011
- 384 Bromirski, P. D., Chen, Z., Stephen, R. A., Gerstoft, P., Arcas, D., Diez, A., ...
 385 Nyblade, A. (2017). Tsunami and infragravity waves impacting antarctic
 386 ice shelves. *Journal of Geophysical Research: Oceans*, 122(7), 5786-5801.
 387 Retrieved from [https://agupubs.onlinelibrary.wiley.com/doi/abs/](https://agupubs.onlinelibrary.wiley.com/doi/abs/10.1002/2017JC012913)
 388 10.1002/2017JC012913 doi: <https://doi.org/10.1002/2017JC012913>
- 389 Chen, Z., Bromirski, P., Gerstoft, P., Stephen, R., Lee, W. S., Yun, S., ... Nyblade,
 390 A. (2019). Ross ice shelf icequakes associated with ocean gravity wave activity.
 391 *Geophysical Research Letters*, 46(15), 8893–8902.
- 392 Christianson, K., Bushuk, M., Dutrieux, P., Parizek, B. R., Joughin, I. R., Alley,
 393 R. B., ... Holland, D. M. (2016). Sensitivity of pine island glacier to ob-
 394 served ocean forcing. *Geophysical Research Letters*, 43(20), 10,817-10,825.
 395 Retrieved from [https://agupubs.onlinelibrary.wiley.com/doi/abs/](https://agupubs.onlinelibrary.wiley.com/doi/abs/10.1002/2016GL070500)
 396 10.1002/2016GL070500 doi: 10.1002/2016GL070500

- 397 Clerc, F., Minchew, B. M., & Behn, M. D. (2019). Marine ice cliff instability mit-
 398 igated by slow removal of ice shelves. *Geophysical Research Letters*, *46*(21),
 399 12108–12116.
- 400 David Holland, & Robert Bindschadler. (2012). *Observing pine island glacier (pig)*
 401 *ice shelf deformation and fracture using a gps and seismic network*. Interna-
 402 tional Federation of Digital Seismograph Networks. Retrieved from [https://](https://www.fdsn.org/networks/detail/XC.2012/)
 403 www.fdsn.org/networks/detail/XC.2012/ doi: 10.7914/SN/XC.2012
- 404 Ekström, G., Nettles, M., & Abers, G. A. (2003). Glacial earthquakes. *Science*,
 405 *302*(5645), 622–624.
- 406 Ewing, M., & Crary, A. (1934). Propagation of elastic waves in ice. part ii. *Physics*,
 407 *5*(7), 181–184.
- 408 Fretwell, P., Pritchard, H. D., Vaughan, D. G., Bamber, J. L., Barrand, N. E.,
 409 Bell, R., . . . Zirizzotti, A. (2013). Bedmap2: improved ice bed, surface
 410 and thickness datasets for antarctica. *The Cryosphere*, *7*(1), 375–393. Re-
 411 trieved from <https://tc.copernicus.org/articles/7/375/2013/> doi:
 412 10.5194/tc-7-375-2013
- 413 Freund, L. B. (1998). *Dynamic fracture mechanics*. Cambridge university press.
- 414 Gibbons, S. J., & Ringdal, F. (2006, 04). The detection of low magnitude seis-
 415 mic events using array-based waveform correlation. *Geophysical Journal Inter-*
 416 *national*, *165*(1), 149–166. Retrieved from [https://doi.org/10.1111/j.1365-](https://doi.org/10.1111/j.1365-246X.2006.02865.x)
 417 [246X.2006.02865.x](https://doi.org/10.1111/j.1365-246X.2006.02865.x) doi: 10.1111/j.1365-246X.2006.02865.x
- 418 Hammer, C., Ohrnberger, M., & Schlindwein, V. (2015). Pattern of cryospheric seis-
 419 mic events observed at ekström ice shelf, antarctica. *Geophysical Research Let-*
 420 *ters*, *42*(10), 3936–3943.
- 421 Heeszel, D. S., Fricker, H. A., Bassis, J. N., O’Neel, S., & Walter, F. (2014). Seis-
 422 micity within a propagating ice shelf rift: The relationship between icequake
 423 locations and ice shelf structure. *Journal of Geophysical Research: Earth*
 424 *Surface*, *119*(4), 731–744. Retrieved from [https://agupubs.onlinelibrary](https://agupubs.onlinelibrary.wiley.com/doi/abs/10.1002/2013JF002849)
 425 [.wiley.com/doi/abs/10.1002/2013JF002849](https://agupubs.onlinelibrary.wiley.com/doi/abs/10.1002/2013JF002849) doi: 10.1002/2013JF002849
- 426 Hetenyi, M. (1946). *Beams on elastic foundation*. Ann Arbor: University of Michi-
 427 gan Press.
- 428 Hulbe, C. L., LeDoux, C., & Cruikshank, K. (2010). Propagation of long frac-
 429 tures in the ronne ice shelf, antarctica, investigated using a numerical model
 430 of fracture propagation. *Journal of Glaciology*, *56*(197), 459–472. doi:
 431 10.3189/002214310792447743
- 432 Jeong, S., Howat, I. M., & Bassis, J. N. (2016). Accelerated ice shelf rift-
 433 ing and retreat at pine island glacier, west antarctica. *Geophysical Re-*
 434 *search Letters*, *43*(22), 11,720–11,725. Retrieved from [https://agupubs](https://agupubs.onlinelibrary.wiley.com/doi/abs/10.1002/2016GL071360)
 435 [.onlinelibrary.wiley.com/doi/abs/10.1002/2016GL071360](https://agupubs.onlinelibrary.wiley.com/doi/abs/10.1002/2016GL071360) doi:
 436 <https://doi.org/10.1002/2016GL071360>
- 437 Joughin, I., Shapero, D., Dutrieux, P., & Smith, B. (2021). Ocean-induced melt vol-
 438 ume directly paces ice loss from pine island glacier. *Science advances*, *7*(43),
 439 eabi5738.
- 440 Joughin, I., Shapero, D., Smith, B., Dutrieux, P., & Barham, M. (2021). Ice-shelf
 441 retreat drives recent pine island glacier speedup. *Science Advances*, *7*(24),
 442 eabg3080.
- 443 Larour, E., Rignot, E., & Aubry, D. (2004). Modelling of rift propagation on ronne
 444 ice shelf, antarctica, and sensitivity to climate change. *Geophysical research let-*
 445 *ters*, *31*(16).
- 446 Lipovsky, B. P. (2018). Ice shelf rift propagation and the mechanics of wave-induced
 447 fracture. *Journal of Geophysical Research: Oceans*, *123*(6), 4014–4033. doi:
 448 <https://doi.org/10.1029/2017JC013664>
- 449 Lipovsky, B. P. (2020). Ice shelf rift propagation: stability, three-dimensional effects,
 450 and the role of marginal weakening. *The Cryosphere*, *14*(5), 1673–1683. doi:
 451 10.5194/tc-14-1673-2020

- 452 Lipovsky, B. P., & Dunham, E. M. (2015). Vibrational modes of hydraulic fractures:
 453 Inference of fracture geometry from resonant frequencies and attenuation.
 454 *Journal of Geophysical Research: Solid Earth*, *120*(2), 1080–1107.
- 455 MacAyeal, D. R., Okal, E. A., Aster, R. C., & Bassis, J. N. (2009). Seismic observa-
 456 tions of glaciogenic ocean waves (micro-tsunamis) on icebergs and ice shelves.
 457 *Journal of Glaciology*, *55*(190), 193–206.
- 458 MacGregor, J. A., Catania, G. A., Markowski, M. S., & Andrews, A. G. (2012).
 459 Widespread rifting and retreat of ice-shelf margins in the eastern amundsen
 460 sea embayment between 1972 and 2011. *Journal of Glaciology*, *58*(209), 458–
 461 466.
- 462 Mattsson, K., Dunham, E. M., & Werpers, J. (2018). Simulation of acoustic and
 463 flexural-gravity waves in ice-covered oceans. *Journal of Computational Physics*,
 464 *373*, 230–252.
- 465 McGrath, D., Steffen, K., Scambos, T., Rajaram, H., Casassa, G., & Lagos, J. L. R.
 466 (2012). Basal crevasses and associated surface crevassing on the larsen c ice
 467 shelf, antarctica, and their role in ice-shelf instability. *Annals of glaciology*,
 468 *53*(60), 10–18.
- 469 Olinger, S. D., Lipovsky, B. P., Wiens, D. A., Aster, R. C., Bromirski, P. D., Chen,
 470 Z., ... Stephen, R. A. (2019). Tidal and thermal stresses drive seismicity
 471 along a major ross ice shelf rift. *Geophysical Research Letters*, *46*(12), 6644-
 472 6652. Retrieved from [https://agupubs.onlinelibrary.wiley.com/doi/abs/](https://agupubs.onlinelibrary.wiley.com/doi/abs/10.1029/2019GL082842)
 473 [10.1029/2019GL082842](https://doi.org/10.1029/2019GL082842) doi: 10.1029/2019GL082842
- 474 Paparrizos, J., & Gravano, L. (2016, June). K-shape: Efficient and accurate cluster-
 475 ing of time series. *SIGMOD Rec.*, *45*(1), 69–76. Retrieved from [https://doi](https://doi.org/10.1145/2949741.2949758)
 476 [.org/10.1145/2949741.2949758](https://doi.org/10.1145/2949741.2949758) doi: 10.1145/2949741.2949758
- 477 Pitz, W., & Miller, D. (2010). The terrasars-x satellite. *IEEE Transac-*
 478 *tions on Geoscience and Remote Sensing*, *48*(2), 615-622. doi: 10.1109/
 479 TGRS.2009.2037432
- 480 Renshaw, C. E., & Schulson, E. M. (2001). Universal behaviour in compressive fail-
 481 ure of brittle materials. *Nature*, *412*(6850), 897–900.
- 482 Rist, M., Sammonds, P., Oerter, H., & Doake, C. (2002). Fracture of antarctic shelf
 483 ice. *Journal of Geophysical Research: Solid Earth*, *107*(B1), ECV–2.
- 484 Scambos, T. A., Bell, R. E., Alley, R. B., Anandkrishnan, S., Bromwich, D., Brunt,
 485 K., ... others (2017). How much, how fast?: A science review and outlook for
 486 research on the instability of antarctica’s thwaites glacier in the 21st century.
 487 *Global and Planetary Change*, *153*, 16–34.
- 488 Sergienko, O. (2017, 07). Behavior of flexural gravity waves on ice shelves: Applica-
 489 tion to the ross ice shelf. *Journal of Geophysical Research: Oceans*, *122*. doi:
 490 [10.1002/2017JC012947](https://doi.org/10.1002/2017JC012947)
- 491 Seroussi, H., Nowicki, S., Payne, A. J., Goelzer, H., Lipscomb, W. H., Abe-Ouchi,
 492 A., ... others (2020). Ismip6 antarctica: a multi-model ensemble of the
 493 antarctic ice sheet evolution over the 21st century. *The Cryosphere*, *14*(9),
 494 3033–3070.
- 495 Shean, D. E., Joughin, I. R., Dutrieux, P., Smith, B. E., & Berthier, E. (2019). Ice
 496 shelf basal melt rates from a high-resolution digital elevation model (dem)
 497 record for pine island glacier, antarctica. *The Cryosphere*, *13*(10), 2633–2656.
 498 Retrieved from <https://tc.copernicus.org/articles/13/2633/2019/> doi:
 499 [10.5194/tc-13-2633-2019](https://doi.org/10.5194/tc-13-2633-2019)
- 500 Shepherd, A., Ivins, E., Rignot, E., Smith, B., Van Den Broeke, M., Velicogna, I.,
 501 ... others (2018). Mass balance of the antarctic ice sheet from 1992 to 2017.
 502 *Nature*, *558*, 219–222.
- 503 Squire, V. A., & Allan, A. (1977). *Propagation of flexural gravity waves in sea*
 504 *ice*. Centre for Cold Ocean Resources Engineering, Memorial University of
 505 Newfoundland.
- 506 Stanton, T. P., Shaw, W., Truffer, M., Corr, H., Peters, L., Riverman, K., ... Anan-

- 507 dakrishnan, S. (2013). Channelized ice melting in the ocean boundary layer
508 beneath pine island glacier, antarctica. *Science*, *341*(6151), 1236–1239.
- 509 Von der Osten-Woldenburg, H. (1990). Icequakes on ekström ice shelf near atka bay,
510 antarctica. *Journal of Glaciology*, *36*(122), 31–36.
- 511 Walker, C., & Gardner, A. (2019). Evolution of ice shelf rifts: Implications for for-
512 mation mechanics and morphological controls. *Earth and Planetary Science*
513 *Letters*, *526*, 115764. Retrieved from <https://www.sciencedirect.com/science/article/pii/S0012821X1930456X> doi: <https://doi.org/10.1016/j.epsl.2019.115764>
- 514
515
- 516 Weertman, J. (1973). Can a water-filled crevasse reach the bottom surface of a
517 glacier. *IASH publ*, *95*, 139–145.
- 518 Williams, R., & Robinson, E. (1981). Flexural waves in the ross ice shelf. *Journal of*
519 *Geophysical Research: Oceans*, *86*(C7), 6643–6648.
- 520 Winberry, J. P., Huerta, A. D., Anandakrishnan, S., Aster, R. C., Nyblade, A. A.,
521 & Wiens, D. A. (2020). Glacial earthquakes and precursory seismicity as-
522 sociated with thwaites glacier calving. *Geophysical Research Letters*, *47*(3),
523 e2019GL086178. Retrieved from <https://agupubs.onlinelibrary.wiley.com/doi/abs/10.1029/2019GL086178> (e2019GL086178 2019GL086178) doi:
524 10.1029/2019GL086178
525
- 526 Zhan, Z., Tsai, V. C., Jackson, J. M., & Helmberger, D. (2014). Ambient noise cor-
527 relation on the amery ice shelf, east antarctica. *Geophysical Journal Interna-*
528 *tional*, *196*(3), 1796–1802.